nature communications

Article

https://doi.org/10.1038/s41467-024-50815-x

Narrowband clusteroluminescence with 100% quantum yield enabled by through-space conjugation of asymmetric conformation

Received: 12 March 2024

Accepted: 22 July 2024

Published online: 30 July 2024

Check for updates

Yipu Wang[1,2,7], Jianyu Zhang[3,7], Qingyang Xu[1,2,4,7], Weihao Tu[1,2,4], Lei Wang[1,2], Yuan Xie[1,2], Jing Zhi Sun[1,4], Feihe Huang[2,5], Haoke Zhang[1,2,4] ✉ & Ben Zhong Tang[1,3,6] ✉

Different from traditional organic luminescent materials based on covalent delocalization, clusteroluminescence from nonconjugated luminogens relies on noncovalent through-space conjugation of electrons. However, such spatial electron delocalization is usually weak, resulting in low luminescent efficiency and board emission peak due to multiple vibrational energy levels. Herein, several nonconjugated luminogens are constructed by employing biphenyl as the building unit to reveal the structure-property relationship and solve current challenges. The intramolecular through-space conjugation can be gradually strengthened by introducing building units and stabilized by rigid molecular skeleton and multiple intermolecular interactions. Surprisingly, narrowband clusteroluminescence with full width at half-maximum of 40 nm and 100% efficiency is successfully achieved via an asymmetric conformation, exhibiting comparable performance to the traditional conjugated luminogens. This work realizes highly efficient and narrowband clusteroluminescence from nonconjugated luminogens and highlights the essential role of structural conformation in manipulating the photophysical properties of unconventional luminescent materials.

The natural world follows a basic principle of modular assembly, where amino acids are assembled into peptides and proteins and eventually into organisms[1–3]. Similarly, benzene rings can be constructed into graphene and carbon nanotubes with unique functional properties[4–7]. The modular assembly usually endows materials with different properties and behaviors compared to individual building units[8–10]. Currently, the construction of organic luminescent materials is typically achieved by covalently linking building units or incorporating donor-acceptor units, where changes in their properties are primarily induced by electron delocalization or charge-transfer effect[11–17].

[1]MOE Key Laboratory of Macromolecular Synthesis and Functionalization, Department of Polymer Science and Engineering, Zhejiang University, Hangzhou 310058, China. [2]Zhejiang-Israel Joint Laboratory of Self-Assembling Functional Materials, ZJU-Hangzhou Global Scientific and Technological Innovation Center, Zhejiang University, Hangzhou 311215, China. [3]Department of Chemistry, Hong Kong Branch of Chinese National Engineering Research Center for Tissue Restoration and Reconstruction, The Hong Kong University of Science and Technology, Hong Kong 999077, China. [4]Centre of Healthcare Materials, Shaoxing Institute, Zhejiang University, Shaoxing 312000, China. [5]Stoddart Institute of Molecular Science, Department of Chemistry, Zhejiang University, Hangzhou 310058, China. [6]School of Science and Engineering, Shenzhen Institute of Aggregate Science and Technology, The Chinese University of Hong Kong, Shenzhen (CUHK-SZ), Guangzhou 518172, China. [7]These authors contributed equally: Yipu Wang, Jianyu Zhang, Qingyang Xu.
✉e-mail: zhanghaoke@zju.edu.cn; tangbenz@cuhk.edu.cn

However, in recent years, researchers have observed that specific nonconjugated small molecules and polymers do not exhibit luminescence in solution but emit intense light after forming clusters, known as clusteroluminescence (CL)[18–20]. The working mechanism of CL has been revealed to be through-space conjugation (TSC) of electrons between isolated building units[21,22]. Using common polyesters as an example, their building units (carbonyl or ester) are connected through spatial *n*–*n* interactions, allowing the formation of TSC and the generation of extrinsic long-wavelength fluorescence[23–25]. Due to the poorly conjugated and flexible structure, these materials possess excellent structural flexibility, processability, biocompatibility, and degradability[26–29]. These advantages show significant implications for developing novel luminescent materials and hold particular value for practical applications[30,31].

Currently, the development of TSC-based emitters has gained considerable attention from researchers[32,33]. However, creating CL materials with exceptional performance that meet application requirements remains a significant challenge[34,35]. The production of CL relies on noncovalent electron overlap and coupling of each unit, which requires the structural flexibility of molecules to form close interactions of electrons in the excited state[36,37]. Therefore, many reported nonconjugated luminogens, such as triphenylmethane and tetraphenylethane, are constructed by rigid building units, which rely on the flexibility of the molecular skeleton to form suitable conformation for TSC[38,39]. However, these luminescent materials based on TSC encounter several issues, including unclear manipulation strategies due to vague structure-property relationship, low luminescent efficiency due to structural flexibility and excited-state molecular motions, as well as broad emission peaks with large full-width at half-maximum (FWHM) values due to numerous vibrational energy levels[40–43]. These challenges present significant obstacles to developing efficient CL materials with high purity of emissive color[44–46]. To address these challenges, one approach is to transfer the flexibility from the molecular skeleton to the building units, forming TSC via the flexibility of building units while maintaining the structural rigidity of the molecular skeleton[47–49]. By achieving strong TSC while minimizing vibrational motions upon photoexcitation, it is possible to achieve narrowband CL with high luminescent efficiency[50–52].

In this work, the simplest biphenyl (BP) is employed as the flexible building unit to construct a series of nonconjugated luminogens, and the structure-property relationship of TSC and CL is systematically studied via two molecule-engineering methods: gradually introducing building units and constitutionally adjusting the connecting positions of building units (Fig. 1). The former suggests the feasibility of using biphenyl as the building unit to enhance the strength of TSC, and the latter indicates the role of structural conformation in intra- and intermolecular interactions, which manipulate the stability of intramolecular TSC for CL. Interestingly, the inspiring example of narrowband CL with an FWHM of 40 nm and 100% efficiency is successfully achieved via an asymmetric triarylmethane, which is comparable to the traditional conjugated narrowband luminogens. This work realizes the narrowband CL from nonconjugated luminogens with isolated biphenyls and provides a perspective to manipulate TSC for unconventional luminescent materials with high efficiency.

Results

According to the above strategy, five compounds, 4-benzhydryl-1,1′-biphenyl (BPM), 4,4″-(phenylmethylene)di-1,1′-biphenyl (DBPM), tri([1,1′-biphenyl]-4-yl)methane (*p*-TBPM), tri([1,1′-biphenyl]-3-yl) methane (*m*-TBPM), tri([1,1′-biphenyl]-2-yl)methane (*o*-TBPM) have been synthesized and fully characterized by using nuclear magnetic resonance spectra, high-resolution mass spectra, and high-performance liquid chromatography techniques (Supplementary Figs. 1–32). UV-visible absorption spectra of the building unit (e.g., BP) and the synthesized BPM, DBPM, and *p*-TBPM were performed in tetrahydrofuran (THF) solutions with different concentrations. The maximum absorption wavelength (λ_{abs}) of biphenyl is located at 249 nm (Supplementary Fig. 33), suggesting its intrinsic through-bond conjugation. However, the λ_{abs} of BPM, DBPM, and *p*-TBPM are quite close to that of biphenyl (259 nm, 260 nm, and 263 nm, respectively), indicating their nonconjugated structures. It is noteworthy that the slight redshift is caused by the hyperconjugation between the π units and the middle saturated carbon. Moreover, the absorption peak does not show an obvious change after aggregation, suggesting that the electronic structure in the ground state remains unchanged during aggregation (Supplementary Figs. 34–37).

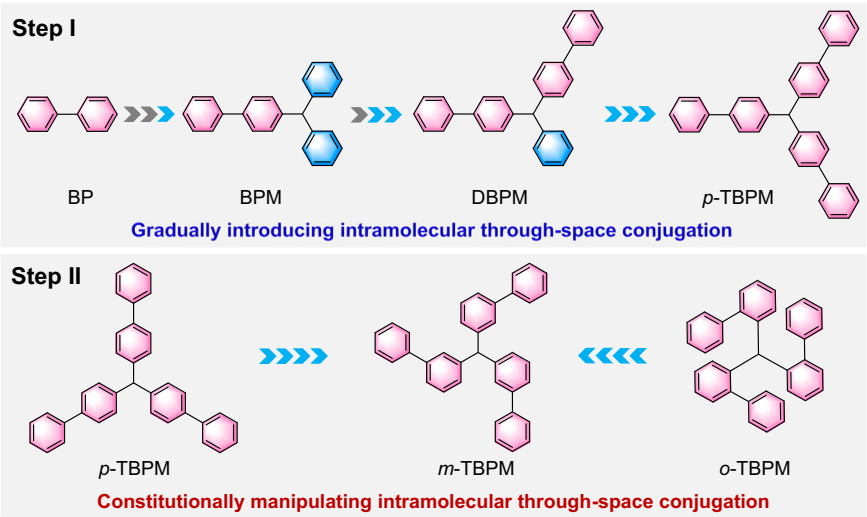

Fig. 1 | The design strategy of nonconjugated molecules with narrowband clusteroluminescence using biphenyl as the building unit. Step I: Gradually introducing intramolecular through-space conjugation by increasing the number of biphenyl subunits; Step II: Constitutionally manipulating intramolecular through-space conjugation by adjusting the connecting positions of biphenyl subunit.

https://doi.org/10.1038/s41467-024-50815-x

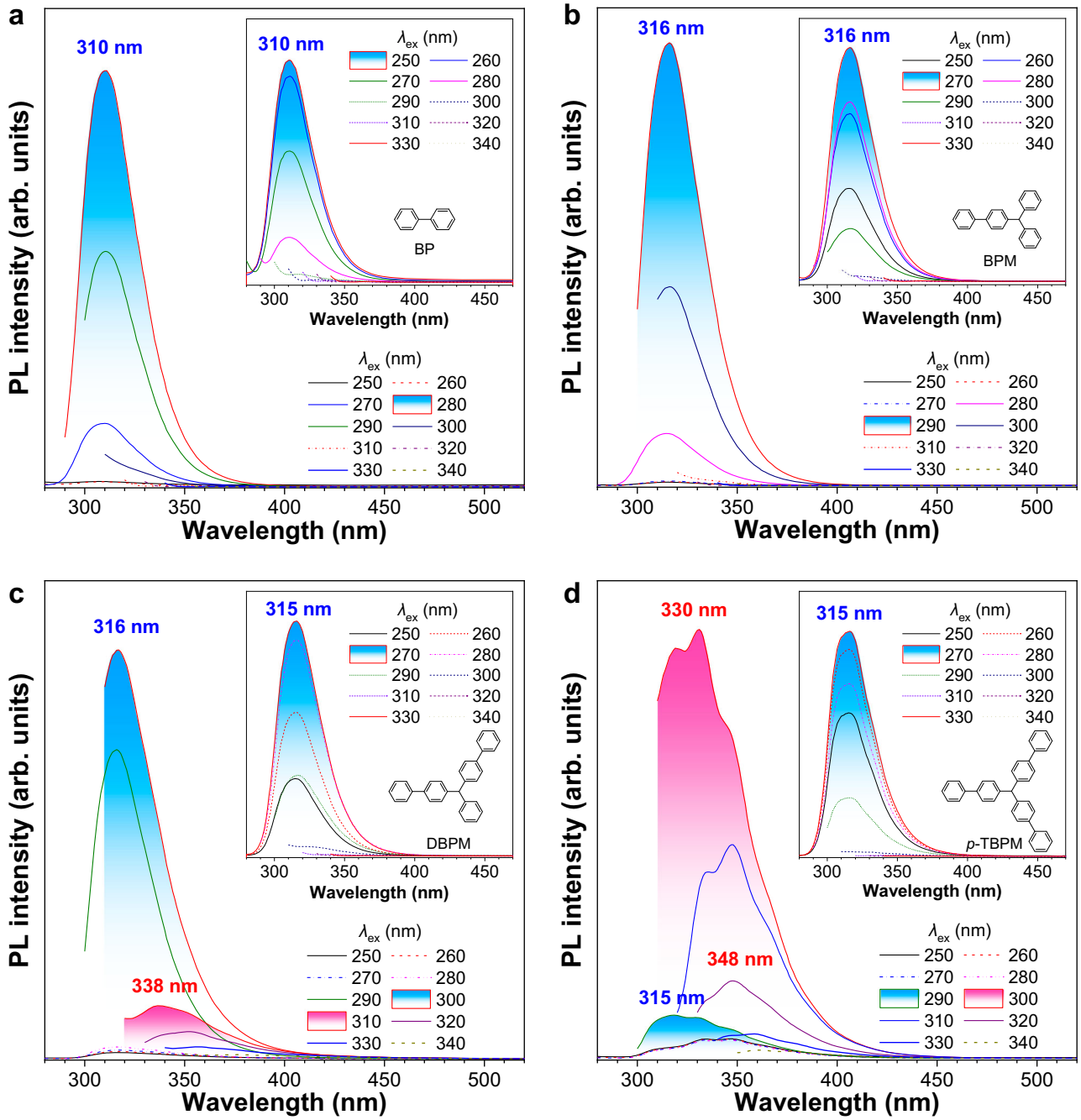

Fig. 2 | Photophysical properties of BP, BPM, DBPM, and *p*-TBPM under different excitation wavelengths. a Photoluminescence (PL) spectra of BP in THF solution (concentration = 10^{-3} M) under different excitation wavelengths. **b** Photoluminescence (PL) spectra of BPM in THF solution (concentration = 10^{-3} M) under different excitation wavelengths. **c** Photoluminescence (PL) spectra of DBPM in THF solution (concentration = 10^{-3} M) under different excitation wavelengths. **d** Photoluminescence (PL) spectra of *p*-TBPM in THF solution (concentration = 10^{-3} M) under different excitation wavelengths. Inset: PL spectra of the corresponding compound in THF solution with a concentration of 10^{-5} M.

Then, the photoluminescence (PL) properties of these compounds were examined in THF solution with different concentrations. Figure 2a and Supplementary Fig. 38 demonstrate that BP exhibits only one emission peak at 310 nm, and the position of the peak remains unchanged with varying concentrations. Similar to BP, BPM displays only one intrinsic emission peak at about 316 nm in different concentrations, which is also attributed to the biphenyl unit (Fig. 2b and Supplementary Fig. 39). In contrast, DBPM exhibits a different behavior compared to the previous two compounds. It shows only one intrinsic emission peak from the biphenyl unit with a low concentration, but long-wavelength emission peaks at 352 nm and 338 nm appears with a high concentration (Fig. 2c and Supplementary Fig. 40). According to previous reports, it should arise from the intramolecular TSC between two isolated biphenyl units of DBPM. Compared to DBPM, *p*-TBPM already exhibits a distinct long-wavelength emission peak at 348 nm in THF solution with a concentration of 10^{-4} M (Supplementary Fig. 41). Moreover, the long-wavelength emission peaks become dominant when the concentration is increased, indicating that *p*-TBPM has the strongest intramolecular TSC among these four compounds (Fig. 2d).

To investigate changes in CL behaviors of these compounds before and after aggregate formation, their PL spectra were further measured

https://doi.org/10.1038/s41467-024-50815-x

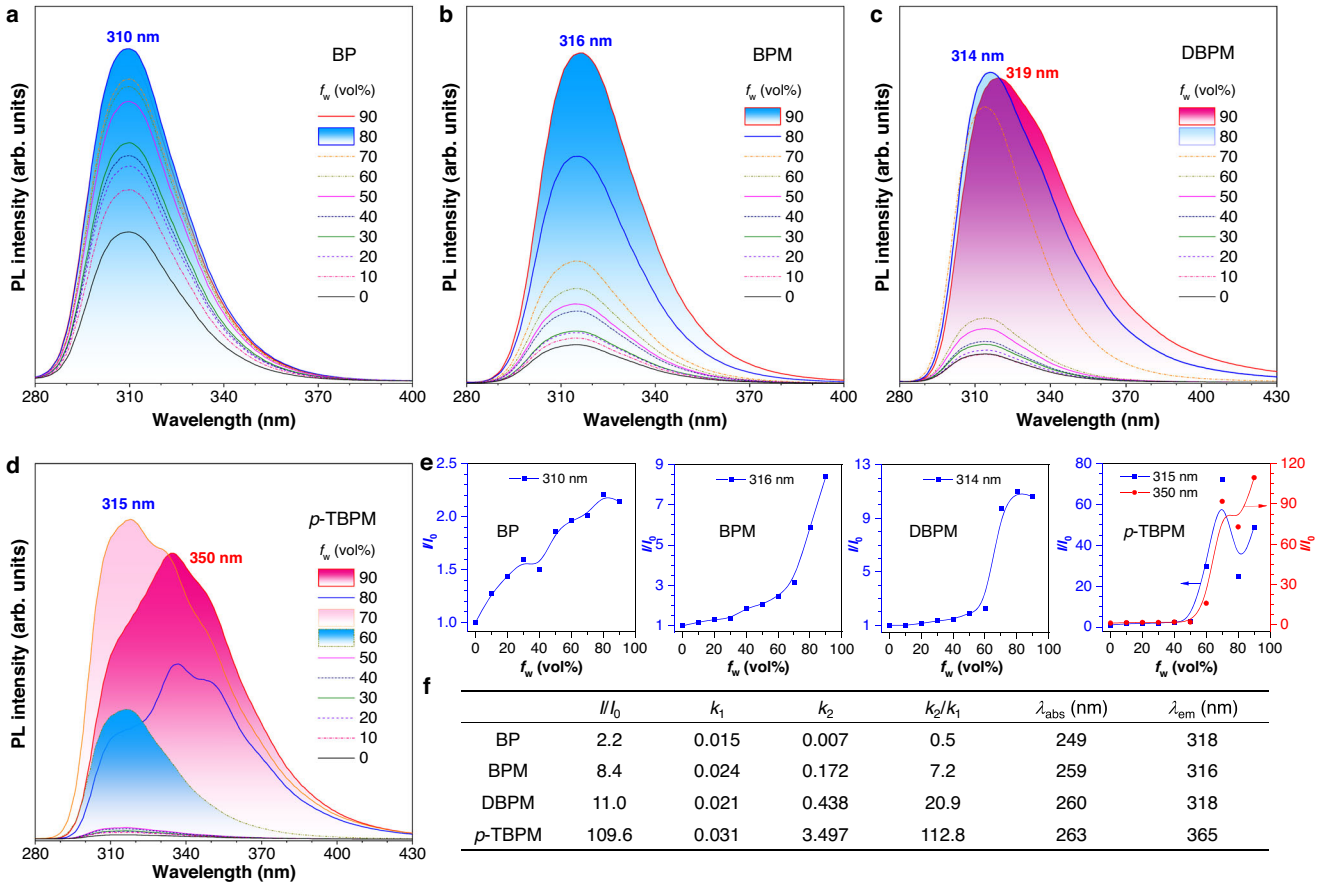

	I/I_0	k_1	k_2	k_2/k_1	λ_{abs} (nm)	λ_{em} (nm)
BP	2.2	0.015	0.007	0.5	249	318
BPM	8.4	0.024	0.172	7.2	259	316
DBPM	11.0	0.021	0.438	20.9	260	318
p-TBPM	109.6	0.031	3.497	112.8	263	365

Fig. 3 | Photophysical properties of BP, BPM, DBPM, and *p*-TBPM before and after aggregate formation. a Photoluminescence (PL) spectra of BP in THF/water mixtures with different water fractions (f_w), concentration (c) = 10^{-4} M, excitation wavelength (λ_{ex}) = 250 nm. **b** Photoluminescence (PL) spectra of BPM in THF/water mixtures with different water fractions (f_w), concentration (c) = 10^{-4} M, λ_{ex} = 260 nm. **c** Photoluminescence (PL) spectra of DBPM in THF/water mixtures with different water fractions (f_w), concentration (c) = 10^{-4} M, λ_{ex} = 260 nm. **d** Photoluminescence (PL) spectra of *p*-TBPM in THF/water mixtures with different water fractions (f_w), concentration (c) = 10^{-4} M, λ_{ex} = 260 nm. **e** Plots of relative PL intensity (I/I_0) *versus* f_w of four compounds. I_0 = intensity at f_w = 0%. **f** Summary of photophysical properties of four compounds. k_1 is the slope of I/I_0 with f_w from 0% – 60%; k_2 is the slope of I/I_0 with f_w from 60% to 90%; λ_{abs} is the maximum absorption wavelength in THF solution; λ_{em} is the maximum emission wavelength in the solid state.

in THF/water mixtures with different water fractions (f_w) and the same concentration of 10^{-4} M. As expected, both BP and BPM only exhibit enhanced emission intensity with the increased f_w (Fig. 3a and b). Besides, the PL spectra of solid-state BP and BPM also show the intrinsic emission at 318 nm and 316 nm, respectively, indicating no formation of intramolecular TSC (Supplementary Fig. 42a and 42b). However, the photophysical behavior of DBPM in THF/water mixtures is different. When increasing f_w, its PL intensity continuously increased. When f_w reaches 90%, the emission peak redshifts from 315 nm to 319 nm with a vague shoulder peak (Fig. 3c). However, the solid-state PL spectra of DBPM do not exhibit a prominent long-wavelength emission peak (Supplementary Fig. 42c). These results indicate that the intramolecular TSC in DBPM is slightly enhanced but still weak. Significantly, the emission intensity of *p*-TBPM at 315 nm gradually increases when f_w increases from 0% to 70%, but the shape of the emission peak changes, and a long-wavelength emission at 350 nm becomes distinct when f_w further increases to >80% (Fig. 3d). As a result, the PL intensity at f_w = 90% is 110 times higher than that in pure THF solution (Fig. 3e). The solid-state PL spectra of *p*-TBPM only shows the long-wavelength emission peak at 365 nm, suggesting the presence of the strongest intramolecular TSC among these four compounds (Supplementary Fig. 42d).

Subsequently, a semi-quantitative analysis was conducted to evaluate the influence of aggregate formation by comparing the slopes of their relative PL intensity (I/I_0) in mixtures (Fig. 3f). k_1 and k_2 are defined as the slopes of PL intensity enhancement before and after the formation of aggregates, respectively, and the ratio of k_2/k_1 represents the enhancement solely induced by aggregation without the influence of the polarity of mixed solvent. It is found that the k_2/k_1 value gradually increases along with the increased numbers of biphenyl units, from BPM of 7.2 to DBPM of 20.9 and *p*-TBPM of 112.8. This result further confirms that the intramolecular TSC could be stepwise enhanced by introducing the flexible building unit of biphenyl, and *p*-TBPM shows the strongest intramolecular TSC among these four compounds.

By gradually introducing biphenyl moieties, we have successfully constructed *p*-TBPM, which exhibits highly efficient CL with an absolute quantum yield (Φ) of 76% (Table 1). However, excitation-dependent emission in the concentrated solution indicates its flexible molecular skeleton and variable TSC. Therefore, *m*-TBPM and *o*-TBPM were designed and synthesized by changing the connecting position of three isolated biphenyl units to study the constitutional manipulation of TSC and structural rigidity (Fig. 1). It was expected that altering the position would adjust the distance and dihedral angle between every biphenyl, thereby manipulating the intramolecular interaction of π electrons and TSC among biphenyl units.

The maximum absorption wavelengths of *m*-TBPM and *o*-TBPM in THF solution are located at 255 nm and 230 nm, respectively, also indicating the nonconjugated nature of three biphenyl moieties as *p*-TBPM (Supplementary Fig. 33). The PL properties of these two

Table 1 | Photophysical properties of *p*-TBPM, *m*-TBPM, and *o*-TBPM[a]

	λ_{abs} (nm)	TBC emission		TSC emission			Φ (%)	k_r (ns^{-1})	k_{nr} (ns^{-1})
		λ_{TBC} (nm)	τ (ns)	λ_{TSC} (nm)	FWHM (nm)	τ (ns)			
p-TBPM	263	–	–	365	53	2.76	76	0.275	0.087
m-TBPM	255	317	4.57	374	40	3.36	100	0.298	–
o-TBPM	230	308	1.49	390	>70	4.43	4	0.009	0.218

[a]Abbreviation: λ_{abs} maximum absorption wavelength in the THF solution, *TBC* through-bond conjugation, *TSC* through-space conjugation, λ_{TBC} maximum emission wavelength of TBC in the solid state, λ_{TSC} maximum emission wavelength of TSC in the solid state, *FWHM* full-width at half-maximum, τ fluorescence lifetime, Φ absolute quantum yield in the solid state. Excitation wavelength: 310 nm for *p*-TBPM and *m*-TBPM, and 300 nm for *o*-TBPM. k_r radiative decay rate, k_{nr} non-radiative decay rate.

compounds were measured and compared. In pure THF solution with a very low concentration of 10^{-6} M, the long-wavelength emission from TSC at about 370 nm is already observable for *m*-TBPM, supporting its ultra-strong intramolecular behaviors (Fig. 4a and Supplementary Fig. 43). Moreover, this observation excludes the possibility of intermolecular TSC, which would otherwise induce long-wavelength emission. Besides, it completely dominates when the concentration reaches 10^{-3} M and becomes excitation-independent, indicating its strong and stable TSC. In THF/water mixtures, the emission originating from TBC displays negligible change when f_w is <60%. As the $f_w \geq 70\%$, the long-wavelength emission from TSC becomes detectable and gradually enhances, reaching an astonishing 136.5 times higher when $f_w = 90\%$ than that in pure THF solution (Fig. 4b). Moreover, the solid-state PL spectra of *m*-TBPM reveal an almost dominant and excitation-independent emission at 374 nm. Surprisingly, the absolute Φ of solid *m*-TBPM reaches 100%, accompanied by a quite narrow peak with the FWHM value of 40 nm, which is attributed to its stable and strengthened TSC with few vibrational energy levels (Fig. 4c and Table 1). To our knowledge, it is of great significance for non-conjugated compounds to produce CL with such a high Φ, and the FWHM is comparable to the conventionally conjugated luminescent materials with narrowband emission[53–55]. Therefore, *m*-TBPM should be a narrowband luminescent material based on the emerging TSC and CL.

Based on the aforementioned design, it was expected that *o*-TBPM would exhibit the strongest intramolecular TSC due to the crowded molecular configuration that may help result in spatial electron delocalization. However, PL results show that only the intrinsic emission from TBC-based biphenyl units is detected at 318 nm in the dilute THF solution of 10^{-5} M, even in the THF/water mixtures with a f_w of 90% (Fig. 4d and e). With the concentration of 10^{-3} M or in the solid state, a weak long-wavelength emission from TSC at 390 nm is observed, while the emission from TBC remains dominant throughout (Fig. 4f and Supplementary Fig. 44). In addition, the quantum yield of solid *o*-TBPM is only 4%, and the FWHM of the long-wavelength emission peak is extremely wide, exceeding 70 nm (Table 1). It could be seen that adjusting the substituents to the *ortho*-position can indeed increase the overlap of delocalized electrons between the isolated units, as evidenced by the extended emission wavelength compared to the other two isomers. However, the crowded conforamtion also reduce the posilibity to generate intramolecular TSC, which will be further investigate by the theortical calcualtion. As a result, *o*-TBPM exhibits the longest emission wavelength of TSC at 390 nm but quite low emission efficiency compared to the other two isomers.

To explore the working mechanism and the difference in the photophysical properties among the three isomers of TBPM, Hirshfeld surface analysis, which is a quantitative analysis of intermolecular interactions based on single-crystal structures, was utilized[56]. As shown in Fig. 5a–c, intermolecular C-C interactions (blue shadows underneath the decomposed plot), which usually result in intermolecular interactions (e.g., π-π stacking) and long-wavelength emission from dimers, account for a negligible proportion of all intermolecular interactions (0.7%, 0.5%, and 0.1% for *p*-TBPM, *m*-TBPM, and *o*-TBPM, respectively). Meanwhile, the crystal packing analysis also indicates the long intermolecular distance between different biphenyl units (Supplementary Figs. 66–68). Thus, the results indicate that there is no obvious strong intermolecular interaction and clearly support the idea that the TSC and CL from these isomers are intramolecular behaviors. In addition, the proportions of weak C-H interactions (contributing to rigidify the aggragte) of *p*-TBPM and *m*-TBPM are 48.6% and 46.5%, respectively, while the proportion of *o*-TBPM is only 27.0% (Supplementary Figs. 62–64), which suggests that *o*-TBPM processes the weakest intermolecular interactions to stabilize its geometry.

Reorganization energy (λ) in the gas phase was analyzed to quantitatively evaluate their intrinsic geometric changes under photoexcitation and the contributions of different intramolecular motions to nonradiative decay (Fig. 5d–f)[57,58]. Among the three isomers, the total λ of *p*-TBPM is the largest (13,268 cm^{-1}), of which 71.60% is contributed by torsional motions of dihedral angles. Therefore, *p*-TBPM processes significant geometric changes that dissipate energy through nonradiative decay in the excited state. Similarly, the total λ of *o*-TBPM is 8322 cm^{-1}, and the contribution from torsional motions of dihedral angles accounts for 55.03%. This result indicates that, unlike its crowded structure which could apparently lead to a rigid conformation, the weak intramolecular TSC in its monodisperse state allows it to retain a certain degree of structural flexibility. Thereby, both the weak intermolecular and intramolecular interactions destroy the formed TSC and endow *o*-TBPM with the smallest Φ of CL in the solid state. Unexpectedly, the total λ of *m*-TBPM is only 1752 cm^{-1}, and the contribution from motions of dihedral angles declines to 30.83%, suggesting its rigid structural conformation and minimized vibrational energy levels. Accordingly, it is believed that the TSC of *m*-TBPM could be stabilized by the stable conformation in both solution and solid states, which endows it to emit strong CL in low-concentration solutions as an isolated luminogen and narrowband CL in the solid state with high purity of color and excitation-independent features (Fig. 4a–f).

For nonconjugated luminogens with CL properties, spatial electron overlap is a typical characteristic. Therefore, hole-electron analysis was applied to study their electronic structure and behaviors in the excited state (Fig. 5g–i). For these three compounds, the hole distribution is located at three isolated biphenyl units. However, electron distribution forms noncovalent delocalization around the central methyl group, forming the typical TSC of electrons that promotes the long-wavelength CL. To provide a quantitative perspective, electron transitions and redistributions from three nonconjugated biphenyl fragments were segmented and compared. Interestingly, *p*-TBPM and *o*-TBPM exhibit electronic behaviors that are different from *m*-TBPM. Three fragments of *p*-TBPM and *o*-TBPM contribute equally to the hole and electron. In contrast, fragment 2 of *m*-TBPM dominates the hole and electron parts with contributions of 46.90% and 46.82%, respectively, while fragments 1 and 3 show smaller and relatively equal contributions (Supplementary Fig. 65a–c). Similarly, the analysis of transferred electrons reveals that the charge delocalization capability

https://doi.org/10.1038/s41467-024-50815-x

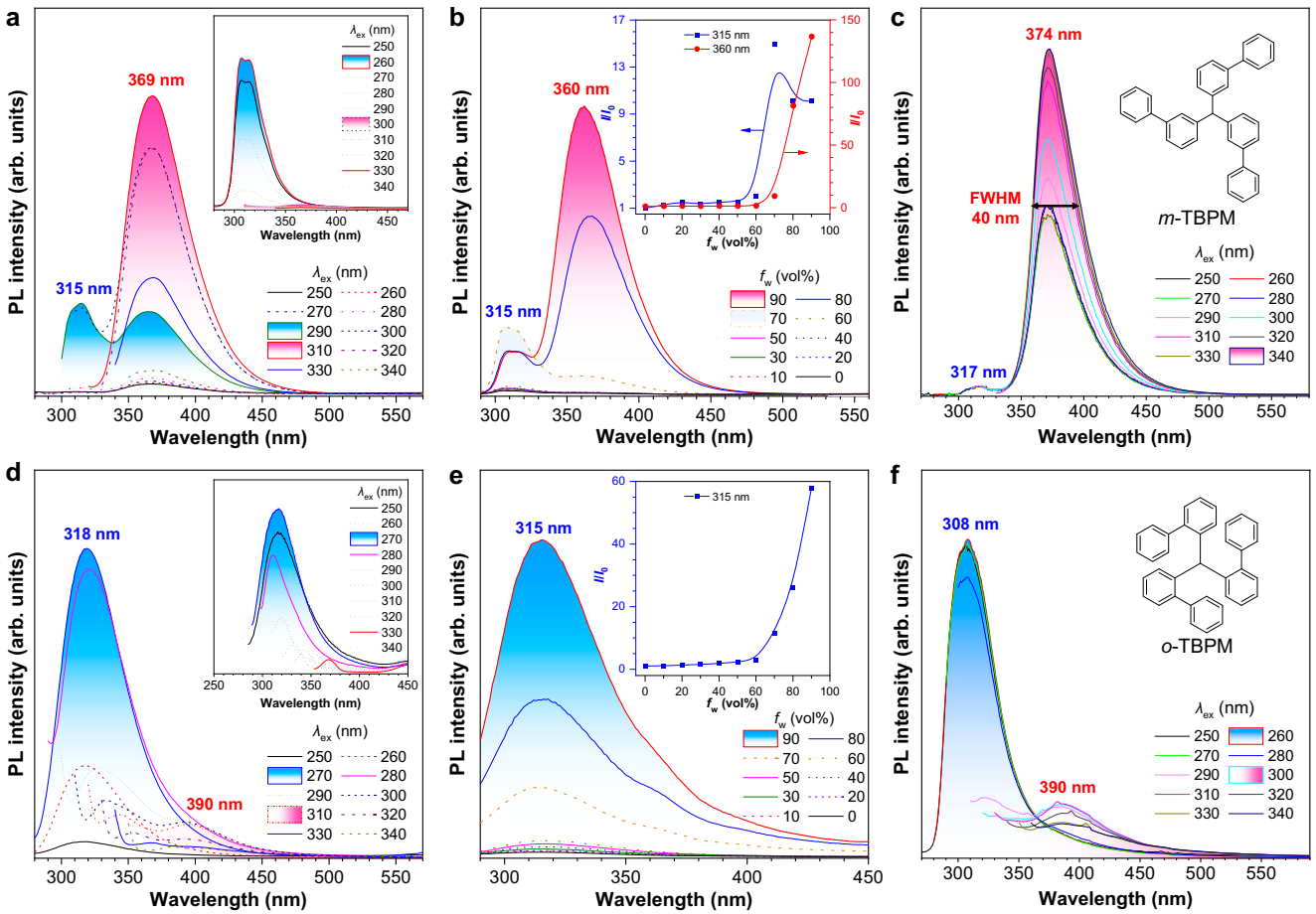

Fig. 4 | Photophysical properties of *m*-TBPM and *o*-TBPM. a Photoluminescence (PL) spectra of *m*-TBPM in THF solution under different excitation wavelengths, concentration (c) = 10^{-3} M. Inset: PL spectra of the corresponding compound in THF solution with a c of 10^{-5} M. **b** PL spectra of *m*-TBPM in THF/water mixtures with different water fractions (f_w), $c = 10^{-4}$ M, excitation wavelength (λ_{ex}) = 260 nm. Inset: Plots of relative PL intensity (I/I_0) versus f_w. I_0 = intensity at f_w = 0%. k_1 is the slope of I/I_0 with f_w from 0% to 60%; k_2 is the slope of I/I_0 with f_w from 60% to 90%. **c** PL spectra of solid-state *m*-TBPM under different excitation wavelengths. **d** Photoluminescence (PL) spectra of *o*-TBPM in THF solution under different excitation wavelengths, concentration (c) = 10^{-3} M. Inset: PL spectra of the corresponding compound in THF solution with a c of 10^{-5} M. **e** PL spectra of *o*-TBPM in THF/water mixtures with different water fractions (f_w), $c = 10^{-4}$ M, λ_{ex} = 230 nm. Inset: Plots of relative PL intensity (I/I_0) versus f_w. I_0 = intensity at f_w = 0%. k_1 is the slope of I/I_0 with f_w from 0% to 60%; k_2 is the slope of I/I_0 with f_w from 60% to 90%. **f** PL spectra of solid-state *o*-TBPM under different excitation wavelengths.

among the three fragments of *p*-TBPM and *o*-TBPM is equal, while fragment 2 of *m*-TBPM exhibits a higher charge delocalization capability (Fig. 5g–i and Supplementary Fig. 65d–f). These results indicate that the structural conformation and formed TSC of *m*-TBPM are asymmetric, which should be also responsible for its highly efficient and narrowband CL.

Based on the above analysis, we have gained insights into the inter-/intramolecular interactions, excited-state molecular motions, and electronic structure that influence the CL of these three isomers. To support the relationship between structural conformation and CL of these nonconjugated compounds, we further revisited their single-crystal structures and packing modes (Supplementary Figs. 66–68). Although the three compounds exhibit symmetric chemical structures with a C3 symmetry axis (Fig. 6a), their conformations of single molecules in the crystalline state differ significantly. Similar to their chemical structures, the conformations of *p*-TBPM and *o*-TBPM are close to symmetric. In contrast, the conformation of crystalline *m*-TBPM is asymmetric (Fig. 6b). Within the packing mode of *p*-TBPM, although there are many intermolecular interactions that could restrict intramolecular motions (Supplementary Fig. 66), its flexible skeleton cannot sufficiently stabilize the formed TSC, endowing it with moderate Φ and FWHM of CL in the crystalline state. For *o*-TBPM, the intermolecular interactions are quite limited, and coupled with the weak calculated intramolecular TSC, this results in its lowest Φ of CL (Supplementary Fig. 67). On the other hand, the rigid molecular skeleton and numerous intermolecular interactions of *m*-TBPM block active intramolecular motions and facilitate the formation of stable TSC for highly efficient CL (Supplementary Fig. 68). Notably, no strong intermolecular interactions of π-π stacking for these three compounds are observed, further verifying their intramolecular behaviors for the long-wavelength emission.

Discussion

Accordingly, a complete picture of the working mechanism and different CL properties from these isomers was summarized (Fig. 6c-e). When compounds are excited from the ground state (S_0) to the excited state (S_1), some excitons release energy through the TBC-based radiative channel with short-wavelength emission from biphenyl units. Meanwhile, some excitons could relax to the low-energy state caused by the TSC of three isolated biphenyl groups, emitting long-wavelength CL. It is worth noting that the efficiency of CL is mainly determined by the strength of TSC and the stability of the corresponding conformation. The former mainly focuses on the magnitude of electron communication, and the latter is achieved by the rigid

https://doi.org/10.1038/s41467-024-50815-x

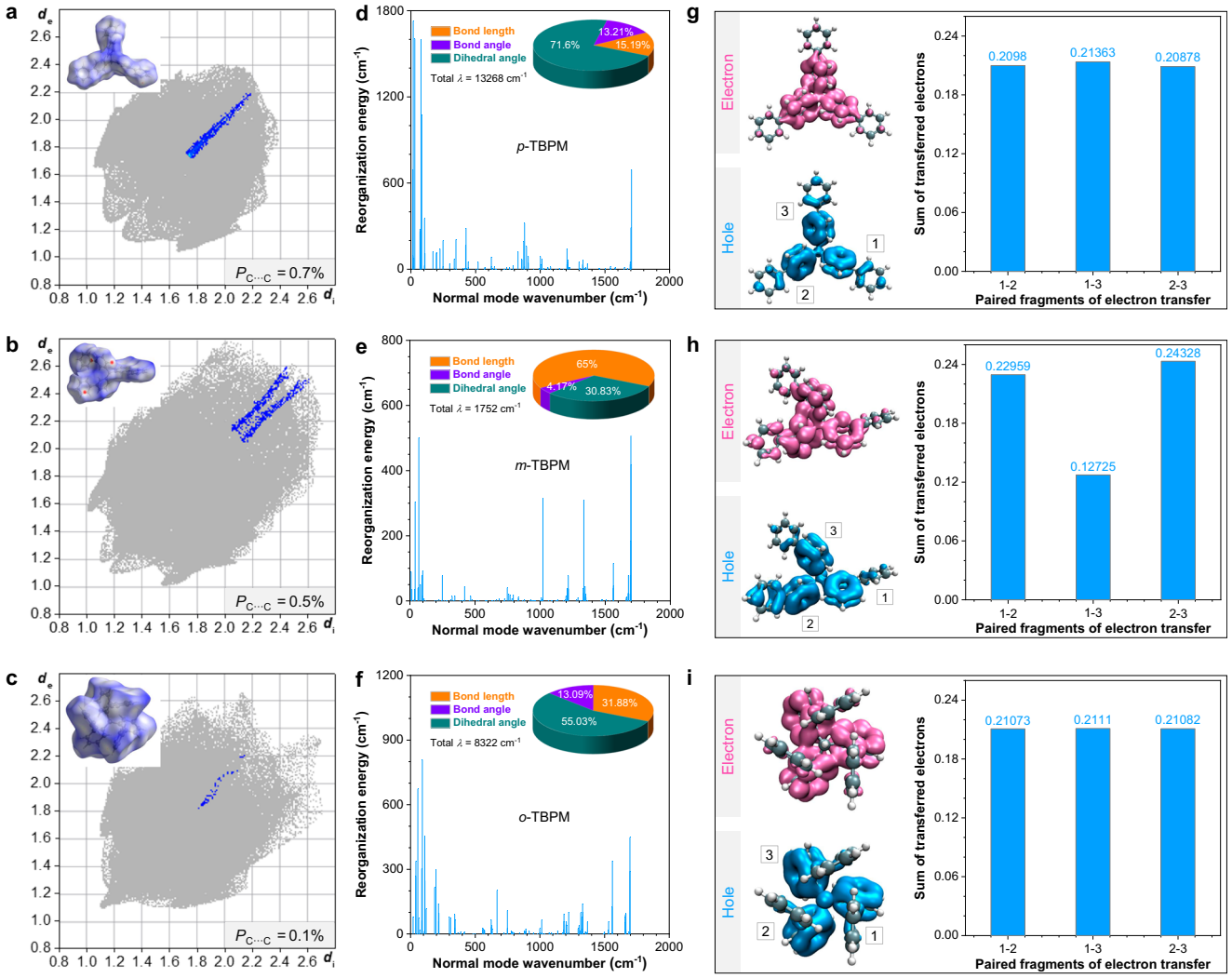

Fig. 5 | Theoretical analysis of *p*-TBPM, *m*-TBPM, and *o*-TBPM. a–c Hirshfeld surfaces (mapped over d_{norm}) and decomposed fingerprint plots of intermolecular C-C interaction of (**a**) *p*-TBPM, (**b**) *m*-TBPM, and (**c**) *o*-TBPM crystals. The full fingerprints appeared as gray shadows underneath decomposed plots, and intermolecular C···C interaction was shown as the blue shadow. $P_{C\cdots C}$ = proportion of intermolecular C···C interactions to total intermolecular interactions. **d**, **e** Plots of reorganization energy *vs* normal mode wavenumber of (**d**) *p*-TBPM, (**e**) *m*-TBPM, and (**f**) *o*-TBPM in the gas phase. **g–i** Hole–electron analysis and transferred electrons of paired fragments of (**g**) *p*-TBPM, (**h**) *m*-TBPM, and (**i**) *o*-TBPM calculated at the M06-2X-D3/6-31 G (d, p) level, Gaussian 16.

molecular skeleton and surrounding environment (e.g., multiple intermolecular interactions). Therefore, conformation plays an essential role in manipulating the CL properties of these isomers. (1) For the structurally symmetric *p*-TBPM, the flexibility of its skeleton allows the formation of TSC upon excitation from the ground state to the excited state. However, its flexible skeleton with active molecular motions cannot be totally restricted via multiple intermolecular interactions, resulting in multiple vibrational energy levels. Therefore, *p*-TBPM produces intrinsic emission from biphenyl units and CL from TSC with a moderate FWHM of 53 nm and comparable Φ of 76% (Fig. 6c). (2) For *m*-TBPM with asymmetric conformation and rigid molecular skeleton, numerous intermolecular interactions can largely stabilize the formed TSC, provide a fixed environment to block molecular motions, and minimize vibrational energy levels[59,60]. As a result, most excitons can relax to the TSC-based state to produce excitation-independent and narrowband CL with an FWHM of 40 nm and a quantitative Φ of 100% in the crystalline state (Fig. 6d). To the best of our knowledge, it is rare that nonconjugated luminogens have achieved 100% quantum yield, and the FWHM value is comparable to reported conjugated compounds with narrowband emission. It is worth noting that TSC-based narrowband emission can also avoid the wide shoulder peaks in some traditional conjugated luminogens with multiple resonance effect (e.g., perylene), further improving the color purity of luminescence[61–63]. (3) For symmetric *o*-TBPM, although the crowded subunits endow it with the largest overlap of electrons to form TSC and the longest wavelength of CL at 390 nm, it also decreases the possibility of forming TSC, in other words, there is an energy barrier to relaxing to the conformation with strong TSC in the excited state. Meanwhile, the weak intermolecular interactions further deactivate the formed TSC. Thus, a small part of excitons relaxes via the TSC-based channel with a board emission peak (FWHM > 70 nm) and a much low Φ of 4% (Fig. 6e).

In this work, biphenyl is utilized as a building block to construct a series of nonconjugated luminogens with CL properties. Two molecule-engineering strategies have been utilized to manipulate TSC and CL: (1) Introducing building blocks of biphenyl units enhances the strength of intramolecular TSC, which promotes the shift of luminescence from the TBC-based channel to the TSC-based CL; (2) Constitutionally adjusting the connection positions of building blocks affects conformation and intermolecular interactions, which regulate

https://doi.org/10.1038/s41467-024-50815-x

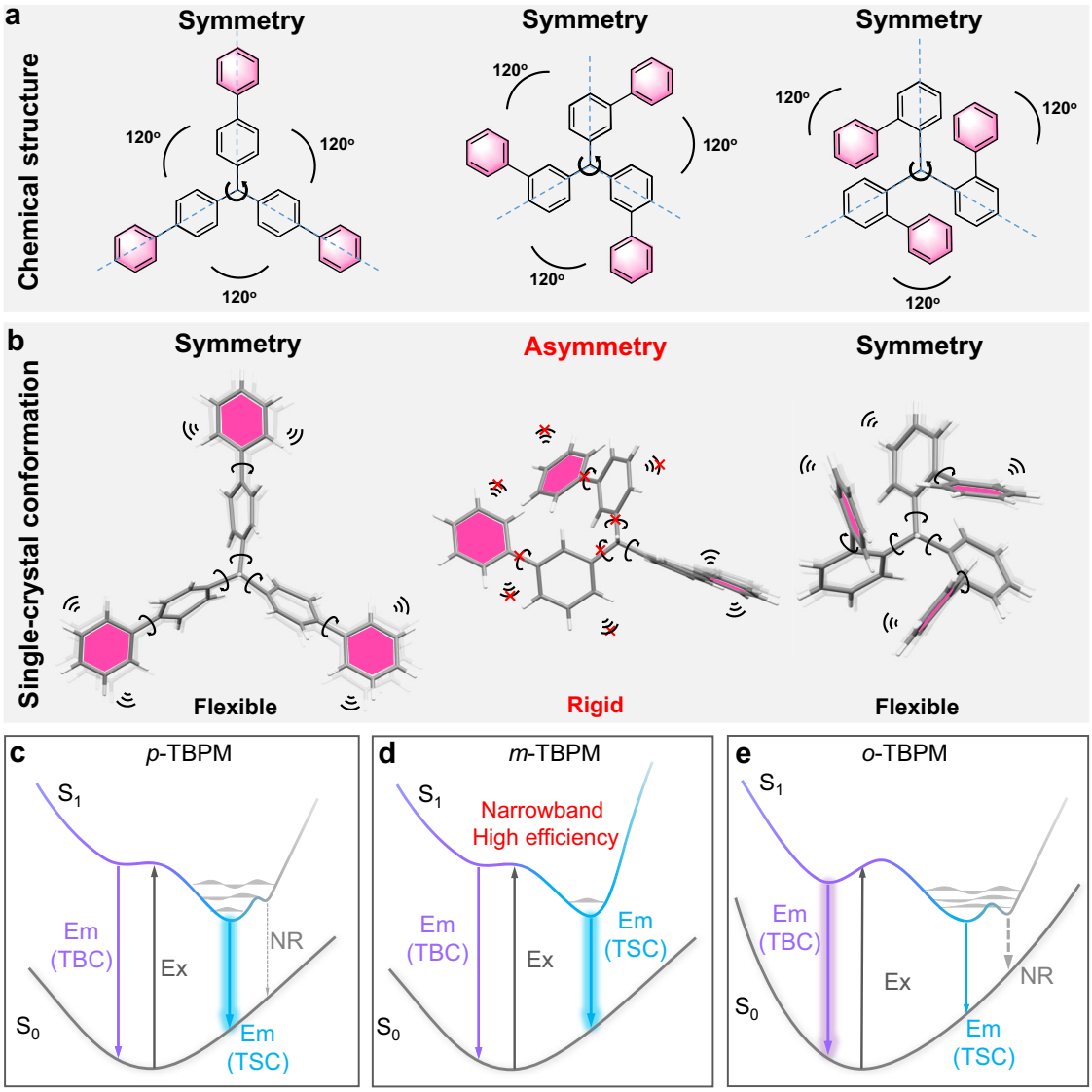

Fig. 6 | Structural analysis of *p*-TBPM, *m*-TBPM, and *o*-TBPM and photoluminescence working mechanism. a Chemical structures of *p*-TBPM, *m*-TBPM, and *o*-TBPM. **b** Structural conformation of *p*-TBPM, *m*-TBPM, and *o*-TBPM in the crystalline state. **c**–**e** Schematic diagram of potential energy surface and electronic behaviors of (**c**) *p*-TBPM, (**d**) *m*-TBPM, and (**e**) *o*-TBPM in the aggregate state.

the stability of TSC and efficiency of CL. Different from the structurally symmetric *p*-TBPM and *o*-TBPM with flexible skeleton, *m*-TBPM with asymmetric conformation exhibits multiple intermolecular interactions and rigid skeleton to promote the formation and stabilization of TSC, achieving narrowband CL with an FWHM of 40 nm and 100% efficiency. The narrowband emission and luminescent efficiency of this nonconjugated compound are highly competitive to traditional luminogens with extended conjugated and planar structures. The emission wavelength of 374 nm may endow it as a near-ultraviolet light source, which could be potentially utilized in manufacturing, photolithography, and maintenance of living organisms. This work highlights the critical role of structural conformation in manipulating the photophysical properties of nonconventional luminescent materials and provides a strategy for developing narrowband CL with improved properties.

Methods

Materials

All chemicals and reagents were purchased from commercial sources such as Bide Pharmatech Ltd., Energy Chemical, Thermo Fisher Scientific, J&K Scientific, and TCI. Common reagents and raw materials were purchased from formal channels, analytically pure, and used without further purification. All the final products used in experiments were purified by silica gel column. The purification of all designed samples was carefully checked by HPLC. Tetrahydrofuran (THF), acetonitrile (ACN), and water used for photophysical measurements were all checked by HPLC.

Instrumentation

^{1}H and ^{13}C nuclear magnetic resonance spectra were recorded on a Bruker AVANCE NEO 600-MHz instrument. UV–vis absorption spectra were recorded by a mid-range UV spectrophotometer (UV-2600i, SHIMADZU). Steady photoluminescence (PL) measurements of all samples were performed on an RF-6000 spectrofluorometer (SHIMADZU) and FLS5 Photoluminescence Spectrometer (Edinburgh Instrument). Fluorescence lifetime was measured by FLS1000 Photoluminescence Spectrometer (Edinburgh Instrument). Absolute fluorescence quantum yields were measured on FLS5 Photoluminescence Spectrometer (Edinburgh Instrument) at least three times. Single-crystal X-ray diffraction (XRD) data were collected on a Rigaku Oxford

Diffraction SuperNova with Atlas Diffractometer (RIGAKU), and crystal structures were solved with Olex2 (a software, https://www.olexsys.org/olex2/). HPLC measurements were carried out on Agilent 1260 Infinity II instrument with Agilent 10 (Prep-C18, 250 × 21.2 mm) column, using THF. High-resolution mass spectra of these compounds were all obtained through Fourier transform mass spectrometry (FTMS), and the test instrument is Thermo Scientific Exactive GC Orbitrap (Thermo Scientific).

Computational details

All the compounds were fully optimized with the density functional theory (DFT) method by using M06-2X density functional and 6-31 G(d,p) basis set. London-dispersion effects were also taken into consideration using Grimme's DFT-D3 correction. Analytical frequency calculations were also performed at the same level of theory to confirm that the optimized structures were at a minimum point. Time-dependent density functional theory (TD-DFT) was utilized at the same level of theory to calculate optimized excited (S_1) geometries and energy levels. All the above quantum chemical calculations were carried out using Gaussian 16 program (Revision A.03)[64]. Reorganization energy analysis was performed using the Molecular Materials Property Prediction Package (MOMAP)[58,65,66]. Besides, the Hirshfeld surfaces and decomposed fingerprint plots were calculated and mapped using CrystalExplorer 17.5 package[56], and the hole-electron analysis were calculated using Multiwfn[67] and displayed using VMD[68].

Data availability

The authors declare that all the data supporting the findings of this manuscript are available within the manuscript and Supplementary Information files and available from the corresponding authors upon request. The Source Data of the coordinates of the optimized geometries are provided. The X-ray crystallographic coordinates for structures reported in this study have been deposited at the Cambridge Crystallographic Data Centre (CCDC) under deposition numbers of *p*-TBPM (2310837), *m*-TBPM (2310838), *o*-TBPM (2310839). These data can be obtained free of charge from The Cambridge Crystallographic Data Centre via www.ccdc.cam.ac.uk/data_request/cif. All data are available from the corresponding author upon request.

References

1. Zhang, X., Li, J., Ma, C., Zhang, H. & Liu, K. Biomimetic structural proteins: modular assembly and high mechanical performance. *Acc. Chem. Res.* **56**, 2664–2675 (2023).
2. Steinhart, M., Wehrspohn, R. B., Gosele, U. & Wendorff, J. H. Nanotubes by template wetting: a modular assembly system. *Angew. Chem. Int. Ed.* **43**, 1334–1344 (2004).
3. Zhang, S. Fabrication of novel biomaterials through molecular self-assembly. *Nat. Biotechnol.* **21**, 1171–1178 (2003).
4. Lu, X. & Chen, Z. F. Curved pi-conjugation, aromaticity, and the related chemistry of small fullerenes (<C60) and single-walled carbon nanotubes. *Chem. Rev.* **105**, 3643–3696 (2005).
5. Yan, L. et al. Chemistry and physics of a single atomic layer: strategies and challenges for functionalization of graphene and graphene-based materials. *Chem. Soc. Rev.* **41**, 97–114 (2012).
6. Bekyarova, E. et al. Effect of covalent chemistry on the electronic structure and properties of carbon nanotubes and graphene. *Acc. Chem. Res.* **46**, 65–76 (2013).
7. Fitzgibbons, T. C. et al. Benzene-derived carbon nanothreads. *Nat. Mater.* **14**, 43–47 (2015).
8. Li, D., Wang, J. & Ma, X. White-light-emitting materials constructed from supramolecular approaches. *Adv. Opt. Mater.* **6**, 1800273 (2018).
9. Takeda, Y., Data, P. & Minakata, S. Alchemy of donor–acceptor–donor multi-photofunctional organic materials: from construction of electron-deficient azaaromatics to exploration of functions. *Chem. Commun.* **56**, 8884–8894 (2020).
10. Duan, L., Qiao, J., Sun, Y. & Qiu, Y. Strategies to design bipolar small molecules for OLEDs: donor-acceptor structure and non-donor-acceptor structure. *Adv. Mater.* **23**, 1137–1144 (2011).
11. Tang, S. et al. Nonconventional luminophores: characteristics, advancements and perspectives. *Chem. Soc. Rev.* **50**, 12616–12655 (2021).
12. Zhang, J. et al. Stimuli-responsive AIEgens. *Adv. Mater.* **33**, 2008071 (2021).
13. Xu, S., Duan, Y. & Liu, B. Precise molecular design for high-performance luminogens with aggregation-induced emission. *Adv. Mater.* **32**, 1903530 (2020).
14. Chen, X., Zhang, X., Xiao, X., Wang, Z. & Zhao, J. Recent developments on understanding charge transfer in molecular electron donor-acceptor systems. *Angew. Chem. Int. Ed.* **62**, e202216010 (2023).
15. Hong, X. et al. TADF molecules with π-extended acceptors for simplified high-efficiency blue and white organic light-emitting diodes. *Chem* **8**, 1705–1719 (2022).
16. Yamaguchi, Y., Matsubara, Y., Ochi, T., Wakamiya, T. & Yoshida, Z. I. How the π conjugation length affects the fluorescence emission efficiency. *J. Am. Chem. Soc.* **130**, 13867–13869 (2008).
17. Yang, J. et al. Constitutional isomerism of the linkages in donor–acceptor covalent organic frameworks and its impact on photocatalysis. *Nat. Commun.* **13**, 6317 (2022).
18. Zhang, H. & Tang, B. Z. Through-space interactions in cluster-oluminescence. *JACS Au* **1**, 1805–1814 (2021).
19. Sakhno, T. V., Sakhno, Y. E. & Kuchmiy, S. Y. Clusteroluminescence of unconjugated polymers: a review. *Theor. Exp. Chem.* **59**, 75–106 (2023).
20. Zheng, S., Zhu, T., Wang, Y., Yang, T. & Yuan, W. Z. Accessing tunable afterglows from highly twisted nonaromatic organic AIEgens via effective through-space conjugation. *Angew. Chem. Int. Ed.* **59**, 10018–10022 (2020).
21. Li, Q. et al. Through-space charge-transfer polynorbornenes with fixed and controllable spatial alignment of donor and acceptor for high-efficiency blue thermally activated delayed fluorescence. *Angew. Chem. Int. Ed.* **59**, 20174–20182 (2020).
22. Zhang, H. et al. Why do simple molecules with "isolated" phenyl rings emit visible light? *J. Am. Chem. Soc.* **139**, 16264–16272 (2017).
23. Chu, B. et al. Aliphatic polyesters with white-light cluster-oluminescence. *J. Am. Chem. Soc.* **144**, 15286–15294 (2022).
24. He, B. et al. Clusteroluminescence from cluster excitons in small heterocyclics free of aromatic rings. *Adv. Sci.* **8**, 2004299 (2021).
25. Li, H. et al. As fiber meets with AIE: opening a wonderland for smart flexible materials. *Adv. Mater.* **35**, 2210085 (2023).
26. Kong, D., Zhang, K., Tian, J., Yin, L. & Sheng, X. Biocompatible and biodegradable light-emitting materials and devices. *Adv. Mater. Technol.* **7**, 2100006 (2022).
27. Liu, J. et al. Through-space interaction of tetraphenylethylene: what, where, and how. *J. Am. Chem. Soc.* **144**, 7901–7910 (2022).
28. Feig, V. R., Tran, H. & Bao, Z. Biodegradable polymeric materials in degradable electronic devices. *ACS Cent. Sci.* **4**, 337–348 (2018).
29. Zhao, D. et al. Cellulose-based flexible functional materials for emerging intelligent electronics. *Adv. Mater.* **33**, 2000619 (2021).
30. Ying, L., Ho, C. L., Wu, H., Cao, Y. & Wong, W. Y. White polymer light-emitting devices for solid-state lighting: materials, devices, and recent progress. *Adv. Mater.* **26**, 2459–2473 (2014).
31. Zhang, Z. et al. Manipulation of clusteroluminescence in carbonyl-based aliphatic polymers. *Aggregate* **3**, e278 (2022).
32. Zhang, J. et al. How to manipulate through-space conjugation and clusteroluminescence of simple AIEgens with isolated phenyl rings. *J. Am. Chem. Soc.* **143**, 9565–9574 (2021).

33. Zhang, H. et al. Clusterization-triggered emission: uncommon luminescence from common materials. *Mater. Today* **32**, 275–292 (2020).
34. Li, J., Shen, P., Zhao, Z. & Tang, B. Z. Through-space conjugation: a thriving alternative for optoelectronic materials. *CCS Chem.* **1**, 181–196 (2019).
35. Liao, P. et al. Generating circularly polarized luminescence from clusterization-triggered emission using solid phase molecular self-assembly. *Nat. Commun.* **12**, 5496 (2021).
36. Li, Q. et al. Pillararene-induced intramolecular through-space charge transfer and single-molecule white-light emission. *Angew. Chem. Int. Ed.* **61**, e202202381 (2022).
37. Viglianti, L. et al. Unusual through-space interactions between oxygen atoms that mediate inverse morphochromism of an AIE luminogen. *Angew. Chem. Int. Ed.* **59**, 8552–8559 (2020).
38. Li, Q. et al. Molecular-level enhanced clusterization-triggered emission of nonconventional luminophores in dilute aqueous solution. *Nat. Comm.* **14**, 409 (2023).
39. Chu, B. et al. Altering chain flexibility of aliphatic polyesters for yellow-green clusteroluminescence in 38 % quantum yield. *Angew. Chem. Int. Ed.* **61**, e202114117 (2022).
40. Zhang, J. et al. Secondary through-space interactions facilitated single-molecule white-light emission from clusteroluminogens. *Nat. Commun.* **13**, 3492 (2022).
41. Zhang, Z. et al. NIR clusteroluminescence of non-conjugated phenolic resins enabled by through-space interactions. *Angew. Chem. Int. Ed.* **62**, e202306762 (2023).
42. Kim, Y. H., Cho, H. & Lee, T. W. Metal halide perovskite light emitters. *Proc. Natl Acad. Sci. USA* **113**, 11694–11702 (2016).
43. Zhao, Z., Zhang, H., Lam, J. W. Y. & Tang, B. Z. Aggregation-induced emission: new vistas at the aggregate level. *Angew. Chem. Int. Ed.* **59**, 9888–9907 (2020).
44. Naveen, K. R., Oh, J. H., Lee, H. S. & Kwon, J. H. Tailoring extremely narrow FWHM in hypsochromic and bathochromic shift of polycyclo-heteraborin MR-TADF materials for high-performance OLEDs. *Angew. Chem. Int. Ed.* **62**, e202306768 (2023).
45. Qu, Y. K. et al. Steric modulation of spiro structure for highly efficient multiple resonance emitters. *Angew. Chem. Int. Ed.* **61**, e202201886 (2022).
46. Liu, J. et al. Toward a BT.2020 green emitter through a combined multiple resonance effect and multi-lock strategy. *Nat. Commun.* **13**, 4876 (2022).
47. Song, B. et al. Facile conversion of water to functional molecules and cross-linked polymeric films with efficient clusteroluminescence. *Nat. Commun.* **14**, 3115 (2023).
48. Zhang, J. et al. White-light emission from organic aggregates: a review. *Adv. Photonics* **4**, 014001 (2021).
49. Shi, C. Y. et al. Dynamic supramolecular H-bonding network with orthogonally tunable clusteroluminescence. *Angew. Chem. Int. Ed.* **62**, e202214422 (2023).
50. Xiong, Z., Zhang, J., Sun, J. Z., Zhang, H. & Tang, B. Z. Excited-state odd–even effect in through-space interactions. *J. Am. Chem. Soc.* **145**, 21104–21113 (2023).
51. Qiu, W. et al. Afterglow OLEDs incorporating bright closely stacked molecular dimers with ultra-long thermally activated delayed fluorescence. *Matter* **6**, 1231–1248 (2023).
52. Madayanad Suresh, S., Hall, D., Beljonne, D., Olivier, Y. & Zysman-Colman, E. Multiresonant thermally activated delayed fluorescence emitters based on heteroatom-doped nanographenes: recent advances and prospects for organic light-emitting diodes. *Adv. Funct. Mater.* **30**, 1908677 (2020).
53. Han, J. et al. Narrowband blue emission with insensitivity to the doping concentration from an oxygen-bridged triarylboron-based TADF emitter: nondoped OLEDs with a high external quantum efficiency up to 21.4%. *Chem. Sci.* **13**, 3402–3408 (2022).
54. Yang, W. et al. An effective approach toward yellow-to-orange multi-resonance TADF emitters by integrating strong electron donor into B/N-Based polycyclic architecture: high performance OLEDs with nearly 40% EQE. *Adv. Funct. Mater.* **33**, 2213056 (2023).
55. Luo, S. et al. Regulation of multiple resonance delayed fluorescence via through-space charge transfer excited state towards high-efficiency and stable narrowband electroluminescence. *Angew. Chem. Int. Ed.* **62**, e202310943 (2023).
56. Spackman, M. A. & Jayatilaka, D. Hirshfeld surface analysis. *CrystEngComm* **11**, 19–32 (2009).
57. Zhang, H. et al. Drawing a clear mechanistic picture for the aggregation-induced emission process. *Mater. Chem. Front.* **3**, 1143–1150 (2019).
58. Shuai, Z. & Peng, Q. Organic light-emitting diodes: theoretical understanding of highly efficient materials and development of computational methodology. *Natl Sci. Rev.* **4**, 224–239 (2017).
59. Tu, W. et al. Manipulation of the through-space interactions in diphenylmethane. *Smart Mol.* **1**, e20220006 (2023).
60. Liu, F. M. et al. Toward narrowband emission: the chemical strategies for modifying boron-based luminescent materials. *J. Mater. Chem. C.* **11**, 11425–11439 (2023).
61. Kondo, Y. et al. Narrowband deep-blue organic light-emitting diode featuring an organoboron-based emitter. *Nat. Photonics* **13**, 678–682 (2019).
62. Naveen, K. R., Hwang, S. J., Lee, H. & Kwon, J. H. Narrow band red emission fluorophore with reasonable multiple resonance effect. *Adv. Electron. Mater.* **8**, 2101114 (2022).
63. Liao, X. J. et al. Planar chiral multiple resonance thermally activated delayed fluorescence materials for efficient circularly polarized electroluminescence. *Angew. Chem. Int. Ed.* **62**, e202217045 (2023).
64. Frisch, M. J. et al. *Gaussian 16,* Vol. 300 (Gaussian, Inc., 2016).
65. Shuai, Z. Thermal vibration correlation function formalism for molecular excited state decay rates. *Chin. J. Chem.* **38**, 1223–1232 (2020).
66. Shuai, Z. & Peng, Q. Excited states structure and processes: understanding organic light-emitting diodes at the molecular level. *Phys. Rep.* **537**, 123–156 (2014).
67. Lu, T. & Chen, F. Multiwfn: a multifunctional wavefunction analyzer. *J. Comput. Chem.* **33**, 580–592 (2012).
68. Humphrey, W., Dalke, A. & Schulten, K. VMD-visual molecular dynamics. *J. Mol. Graph.* **14**, 33–38 (1996).

Acknowledgements

This work was supported by the National Natural Science Foundation of China (22205197) and the China Postdoctoral Science Foundation (2022M712721). J.Z. acknowledged the support from the Research Grants Council of the Hong Kong Special Administrative Region, China (HKUST PDFS2324-6S01).

Author contributions

Y.W., J.Z. and Q.X. performed research, wrote the original draft of the article and carried out theoretical calculation. W.T., L.W., and Y.X. contributed synthesis. J.Z.S. and F.H. participated in the discussion. H.Z. and B.Z.T. contributed to project administration, funding acquisition, and revision of the article.

Competing interests

The authors declare no competing interests.

Additional information

Supplementary information The online version contains supplementary material available at https://doi.org/10.1038/s41467-024-50815-x.

Correspondence and requests for materials should be addressed to Haoke Zhang or Ben Zhong Tang.

Peer review information *Nature Communications* thanks Huiliang Wang, who co-reviewed with Junwen DengJinliang Qiao and the other, anonymous, reviewer for their contribution to the peer review of this work. A peer review file is available.